

# Microstructural Development and Solidification Cracking Susceptibility of a Stabilized Stainless Steel

*Solidification modeling results are utilized to relate fusion zone composition to mushy zone characteristics and resultant solidification cracking susceptibility in Alloy 20Cb-3*

BY J. N. DuPONT

**ABSTRACT.** The solidification behavior and fusion zone solidification cracking response of Alloy 20Cb-3 was investigated by Varestraint testing, differential thermal analysis (DTA) and microstructural characterization techniques including light optical microscopy (LOM), scanning electron microscopy (SEM) and electron probe microanalysis (EPMA). Autogenous 20Cb-3 welds were evaluated, along with composite fusion zones prepared with 20Cb-3 base metal and INCO 112 filler metal. The 20Cb-3 alloy initiated solidification by a primary  $L \rightarrow \gamma$  reaction and completed solidification at  $\sim 1300^\circ\text{C}$  ( $2372^\circ\text{F}$ ) by a eutectic-type  $L \rightarrow (\gamma + \text{NbC})$  transformation. The composite 20Cb-3/INCO 112 fusion zone also exhibited the primary  $L \rightarrow \gamma$  and eutectic-type  $L \rightarrow (\gamma + \text{NbC})$  reactions, but solidification did not terminate until  $1223^\circ\text{C}$  ( $2233.4^\circ\text{F}$ ), with a second eutectic-type reaction consisting of  $L \rightarrow (\gamma + \text{Laves})$ . The solidification paths of each fusion zone composition were calculated and plotted on a  $\gamma$ -Nb-C pseudo-ternary liquidus projection as an aid to understanding the influence of alloy composition on the progression of solidification transformations, and the predicted results were in good agreement with the experimentally determined solidification reaction sequences. Both the autogenous 20Cb-3 and composite 20Cb-3/INCO 112 fusion zones exhibited a higher degree of solidification cracking susceptibility than 304 stainless steel. The 20Cb-3/INCO 112 composite fusion zone displayed the highest cracking propensity. A recently developed model was utilized to calculate the variation in fraction liquid with distance within the crack-susceptible solid + liquid (mushy) zone for each fusion zone

composition. The modeling results directly showed that the presence of the low temperature  $L \rightarrow (\gamma + \text{Laves})$  reaction in the 20Cb-3/INCO 112 fusion zone extended the mushy zone out to large distances, thus accounting for the higher crack lengths observed in this composite fusion zone sample during Varestraint testing. These results were used to understand the relation between fusion zone composition, solidification behavior and the resultant solidification cracking response.

## Introduction

Alloy 20Cb-3 is a high-Ni austenitic stainless steel stabilized with Nb additions and is utilized for aggressive corrosion environments in the chemical and process industries. Because of the high Ni content, the weld metal solidifies in the fully austenitic mode and is, therefore, prone to solidification cracking (Ref. 1). In applications where filler metal is utilized, the alloy was originally welded with the 320 class filler metals, in which no special effort was placed on control of minor elements. Subsequent work by Brown, *et al.* (Ref. 1), showed that the cracking resistance of welds in 20Cb-3 increased when 320 electrodes were used with reductions in Nb, Si and

P, along with increases in Mn. This work led to the development of a 320LR electrode, in which these elemental concentrations were controlled for improved weldability.

The solidification cracking susceptibility of fully austenitic weld metal depends on the solidification temperature range and terminal solidification events that occur at the grain boundaries and interdendritic regions (Refs. 2, 3). This is particularly true for austenitic alloys containing Nb, which are known to form Nb-rich phases such as NbC and Laves at the terminal stages of solidification (Refs. 4–6). These secondary solidification phases typically form in a eutectic-type morphology with the austenite matrix. Of the two possible phases that can form, the Laves phase is known to be more detrimental because it forms at a lower temperature and, thus, widens the solidification temperature range (Refs. 4, 7). The propensity for forming each type of constituent (*i.e.*, NbC and/or Laves) and the resultant solidification cracking susceptibility is highly dependent on the nominal alloy composition (Refs. 4, 8). However, no published data are available that link the solidification behavior of Alloy 20Cb-3 to solidification cracking susceptibility. Thus, in this work, Varestraint weldability evaluations are combined with microstructural characterization and differential thermal analysis results to establish an understanding of solidification behavior/hot cracking relations of Alloy 20Cb-3.

## Experimental Procedure

### Materials

Table 1 lists the chemical compositions of the base metals and shielded metal arc welding (SMAW) electrodes utilized in this work. All of the measured compositions are within the values specified for these alloys. The base metals

### KEY WORDS

Alloy 20 Cb-3  
E320LR  
INCO 112  
Laves Phase  
Maximum Crack Length  
Stainless Steel  
Solidification Cracking  
Varestraint Testing

J. N. DuPONT is Assistant Professor in the Materials Science and Engineering Department, Lehigh University, Bethlehem, Pa.



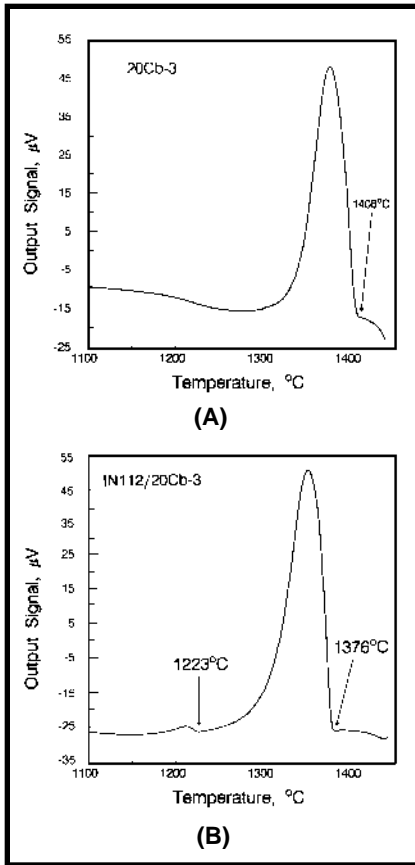


Fig. 3 — DTA cooling curves for: A — 20Cb-3; B — 20Cb-3/INCO 112 composite fusion zone sample.

a light optical microscope (LOM) interfaced with a quantitative image analysis (QIA) system.

#### Differential Thermal Analysis (DTA)

A small sample of all-weld-metal was removed from the 20Cb-3/INCO 112 SMAW fusion zone for differential thermal analysis, by electro-discharge machining. The cross-sectional dimensions required to obtain an all-weld-metal deposit were determined metallographically. The 3.2-mm-thick 20Cb-3 base metal was also evaluated by DTA. The DTA was conducted on a Netzsch STA 409 thermal analyzer, using argon cover gas and an alumina crucible. The sample size was  $\approx 0.65$  gram and pure Ni was used as the reference material. The samples were heated to 1440°C (2624°F) at a rate of 5°C (9°F)/min, at which point they were completely molten. The samples were then cooled at 20°C (36°F)/min through the solidification temperature range. The weight of the sample was simultaneously monitored by a thermogravimetric balance to ensure that no weight change occurred during the test.

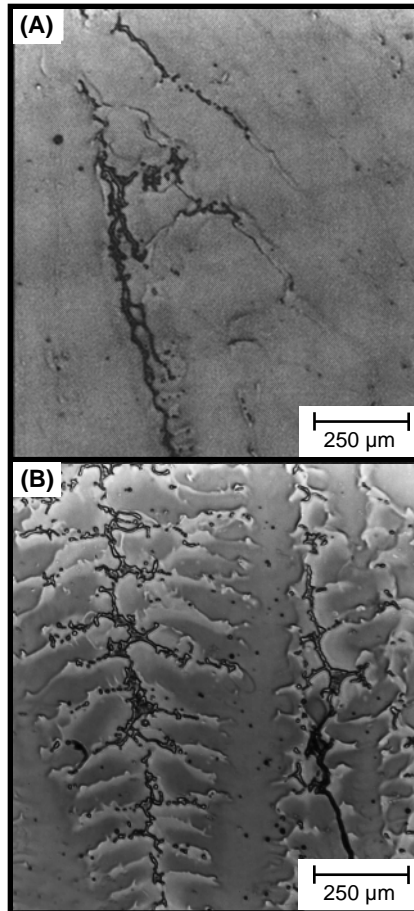


Fig. 4 — Light optical photomicrographs of typical solidification cracks induced by the Varestraint tests in: A — 20Cb-3 autogenous fusion zone; B — 20Cb-3/INCO 112 composite fusion zone.

The DTA system was calibrated by determining the melting temperature of pure Ni and was found to be within 2°C (3.6°F) of the literature value. Consistent with previous work on similar alloy systems, reaction temperatures were taken as deviations from the local baseline (Refs. 4–7).

#### Microstructural Characterization

Specimens were removed from the Varestraint samples for microstructural characterization by light optical microscopy (LOM) and scanning electron microscopy (SEM). The samples were mounted in planar view to examine the solidification cracks, which intersected the sample surface. All samples were polished to a 0.04- $\mu$ m finish using colloidal silica and electrolytically etched at  $\approx 3$  V in a 10% chromic acid/90% water solution. SEM was conducted at 30 kV in the secondary electron mode on carbon-coated samples with a JEOL 6300 field emission gun high-resolution micro-

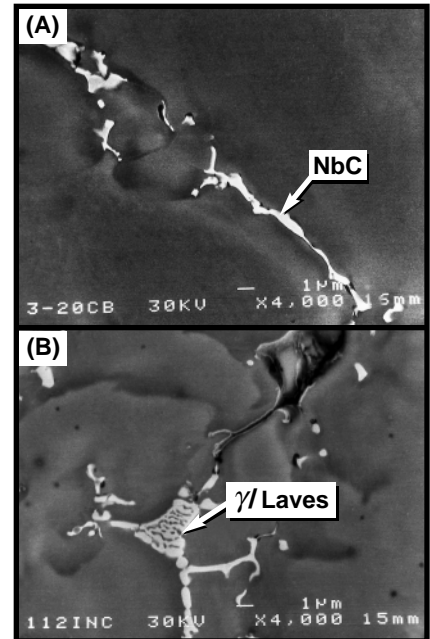


Fig. 5 — Scanning electron photomicrographs of solidification crack tips in: A — 20Cb-3 autogenous fusion zone; B — 20Cb-3/INCO 112 composite fusion zone.

scope. The area fraction of minor constituent in the welds was determined on a LECO 2001 QIA system. Area fraction was assumed to be equal to volume fraction.

A 20Cb-3 autogenous Varestraint sample and a 20Cb-3/INCO 112 composite sample were examined in more detail by electron probe microanalysis (EPMA). The 20Cb-3/INCO 112 composite specimen was examined in the as-deposited condition (*i.e.*, before machining flush with the base metal surface) to obtain an EPMA trace across the entire fusion zone. The objective of this broad trace was to determine the extent (if any) of macrosegregation within the fusion zone of the dissimilar metal weld. For this EPMA trace, the electron beam was scanned over an area of 415  $\mu$ m<sup>2</sup> to smooth out effects from dendritic microsegregation and provide an average composition for the relatively large scan area. This scan was conducted from the fusion line to the surface of the weld. Localized composition gradients due to dendritic microsegregation were also investigated (*i.e.*, with no beam raster). This was accomplished by marking small areas of parallel dendrites on polished and etched samples with a precision microscope scribe. The EPMA samples were then re-polished to a 0.04- $\mu$ m finish and carbon coated. EPMA was conducted on a JEOL 733 microprobe equipped with four wavelength-dispersive spectrom-



**Table 2 — Chemical Composition of 20Cb-3/INCO 112 Fusion Zone as Determined by EPMA Data in Fig. 6 (All values in wt-%)**

Element	Average Fusion Zone Composition
Fe	24.0 ± 0.9
Ni	46.3 ± 1.0
Cr	20.2 ± 0.1
Mo	5.20 ± 0.1
Nb	2.20 ± 0.1
Cu	1.70 ± 0.1
Mn	0.41 ± 0.1
Si	0.36 ± 0.1
C <sup>(a)</sup>	0.014
P <sup>(a)</sup>	0.016
S <sup>(a)</sup>	0.003

(a) Calculated from an average dilution of 0.55.

and INCO 112 electrode, so that macroscopic concentration gradients in the weld are not significant. This result has also been reported in previous work on welds deposited by consumable electrode processes (Refs. 5, 13). Thus, the EPMA data can be used to determine a bulk fusion zone composition. This is presented in Table 2, where the average of EPMA values collected after the 1000 μm position in Fig. 6 are listed.

From the values listed in Table 2, an average dilution value of 0.55 ± 0.05 was determined. The dilution was calculated by

$$D = \frac{E_{fz} - E_{fm}}{E_{bm} - E_{fm}} \quad (1)$$

where E represents the concentration of each element in the fusion zone (fz), filler metal (fm) and base metal (bm). The dilution value determined above from EPMA data is in good agreement with the measured cross-sectional areas of the melted base metal,  $A_{bm}$ , and deposited filler metal  $A_{fm}$ , [Dilution =  $A_{bm}/(A_{bm} + A_{fm})$ ], which yielded a value of 0.50. The dilution value from Equation 1, in turn, can be used to estimate the carbon content in the fusion zone from knowledge of the base metal and filler metal composition and is also listed in Table 2. As explained in the next section, the carbon content in the fusion zone plays a key role in the fusion zone microstructural development and solidification cracking response of these alloys, but when present in such low concentrations, its concentration cannot be accurately determined experimentally by EPMA techniques. Thus, the dilution value is useful for estimating the fusion zone carbon content. Estimated values of the phosphorus and sulfur concentration in the fusion zone are also provided in Table 2, since these elements can be im-

**Table 3 — Typical EPMA Results of NbC and Laves Second Phases Observed in 20Cb-3 Autogenous and 20Cb-3/INCO 112 DTA Samples (All values in wt-%)**

Element	NbC Observed in 20Cb-3 Autogenous Weld and 20Cb-3/INCO 112 Composite Fusion Zone	Laves Observed in 20Cb-3/INCO 112 Composite Fusion Zone
Fe	1.00	12.4
Ni	1.20	31.6
Cr	1.10	12.4
Mo	0.30	16.6
Nb	87.0	23.5
Si	0.70	2.80
Cu	0.25	0.40

portant from a solidification cracking perspective.

Figures 7 and 8 are EPMA traces conducted across several dendrites in the 20Cb-3 autogenous and 20Cb-3/INCO 112 weld metals, respectively. As an example, Fig. 9 shows a region of parallel dendrites that were analyzed by EPMA. Typical examples of dendrite core and interdendritic areas are noted in the EPMA composition traces. For each weld metal type, the dendrite cores are significantly depleted in Mo and Nb. The elements Ni and Cr show very little tendency for microsegregation, while the Fe segregates moderately in the opposite directions of Nb and Mo (*i.e.*, to the dendrite core regions). The behavior of Cu varies. In the Fe-rich 20Cb-3 weld metal, Cu segregates to interdendritic areas rather strongly. In the Ni-rich 20Cb-3/INCO 112 weld, Cu segregates only slightly.

The DTA samples exhibited characteristics similar to the welds where second phases formed in the interdendritic areas. However, as shown in Fig. 10, the second-phase particles were larger due to the slower cooling rates. The 20Cb-3 DTA sample exhibited an isolated secondary phase — Fig. 10A. The 20Cb-3/INCO 112 sample also exhibited this isolated phase, in addition to a large blocky phase that existed in a eutectic-type arrangement with the austenite matrix. The eutectic morphology was not as well developed in the DTA sample shown in Fig. 10B as the weld metal sample shown in Fig. 5B, because of the slower cooling rate of the DTA sample. The size of the secondary phases in the DTA specimens were large enough (≈5–15 μm) to permit chemical analysis by EPMA (resolution ≈1–2 μm), and typical results for each of the phases observed are summarized in Table 3. The Nb content of the isolated second phase in each fusion zone (87 wt-% Nb) is consistent with the NbC phase, which is well known to form during solidification of austenitic alloys

containing Nb and C (Refs. 4, 6, 7, 14, 18). The second phase observed in a eutectic morphology with the austenite matrix, which was found only in the 20Cb-3/INCO 112 fusion zone, had a Nb content of 23.5 wt-%, consistent with the Laves ( $A_2B$ ) phase. As with the NbC phase, it is well established that Laves forms as a secondary solidification constituent in Nb-bearing austenitic alloys (Refs. 4, 6, 7, 14, 18).

## Discussion

### Solidification

The two fusion zone compositions evaluated in this work (20Cb-3 and 20Cb-3/INCO 112) exhibit two types of solidification sequences that are similar to those expected in the simple ternary Ni-Nb-C system (Ref. 15) and recent work conducted on a wide range of experimental multicomponent Nb-bearing superalloys (Ref. 8). The liquidus projection for the Ni-Nb-C system is shown in Fig. 11. The projection exhibits three primary-phase fields that are of interest here: γ, NbC and  $Ni_3Nb$ . A primary C (graphite) phase field exists at high C contents, which is not of importance. Additions of Fe, Cr and Si to the Ni-Nb system are well known to promote Laves at the expense of  $Ni_3Nb$  in commercial superalloys, as well as the experimental alloys utilized in this work (Refs. 16,17). Thus, by replacing  $Ni_3Nb$  with Laves, the Ni-Nb-C liquidus projection can be utilized as a guide in developing a description of the solidification reactions in these alloys.

The 20Cb-3 alloy initiates solidification by formation of primary austenite dendrites (large exothermic peak in the DTA cooling curves). As explained in detail below and documented for other austenitic alloys containing Nb and C (Refs. 6–8, 18), the distribution coefficients (k) for Nb and C are less than unity, indicating that these elements preferentially segregate to the liquid during solid-











